In situ imaging of temperature-dependent fast and reversible nanoscale domain switching in a single-crystal perovskite

Lucas A. B. Marçal [1,2,*] Dmitry Dzhigaev [1] Zhaojun Zhang [1] Ella Sanders,[3] Amnon Rothman,[3] Edoardo Zatterin,[4]
Ewen Bellec,[4] Tobias U. Schülli,[4] Anders Mikkelsen,[1] Ernesto Joselevich [3] and Jesper Wallentin [1]

[1]*Synchrotron Radiation Research and NanoLund, Lund University, Box 118, Lund 22100, Sweden*
[2]*MAX IV Laboratory, Lund University, Lund 22100, Sweden*
[3]*Department of Molecular Chemistry and Materials Science, Weizmann Institute of Science, Rehovot 76100, Israel*
[4]*European Synchrotron Radiation Facility, CS 40220, 38043 Grenoble Cedex 9, France*

Metal halide perovskites exhibit a rich crystal structure, with multiple phases as well as ferroelastic domains, which is crucial for the optical and electrical properties. The average crystal phase-transition temperatures can be shifted by size, strain, or defects, but it is not clear whether such differences can also appear locally within a single crystal. The experimental study of domain dynamics within nanocrystals is challenging and requires a method capable of probing crystal lattice variations with both high spatial and temporal resolution. Here, we show that *in situ* full-field diffraction x-ray microscopy can be used to image domains in a single crystal $CsPbBr_3$ nanoplatelet as the temperature traverses the orthorhombic to tetragonal phase transition, at 150 nm spatial resolution and 6 s time resolution. The images reveal sudden domain pattern changes faster than the temporal resolution. Surprisingly, we observe substantial local variations during heating, with domain changes occurring at different temperatures within the single crystal. The nanoplatelet exhibits a high-temperature domain pattern completely different from the low-temperature one, but both patterns are reproducible, and we reversibly switch between them in multiple cycles. These results demonstrate that single $CsPbBr_3$ crystals can exhibit substantial local variation of their basic crystal properties.

I. INTRODUCTION

The emerging metal halide perovskites (MHPs) show unique optical and electronic properties and have been extensively studied in the last decade for a wide range of potential applications in optoelectronic devices, such as solar cells, light-emitting diodes, and photodetectors [1–5]. The significant research effort on MHP nanocrystals is justified by their simple synthesis and outstanding photoluminescence quantum yield [6–9]. Their optical properties can be affected by changes in the crystal structure [10,11], which makes it crucial, for technological applications, to better understand their basic material properties. Among the MHPs, $CsPbBr_3$ presents good radiation stability, which makes it very promising for applications in optoelectronic devices, including x-ray detectors [12]. At room temperature, bulk $CsPbBr_3$ presents an orthorhombic structure and has two structural phase transitions, one to tetragonal at $88\,°C$ and another one to cubic at $130\,°C$ [13–15]. Previous reports have shown that these

phase-transition temperatures can be changed by strain [16] and defects [17], as wells as size and bulk to surface ratio [7,14,18]. A natural question is then whether such variations could also be present within a single crystal or grain.

The low symmetry of MHP crystal structures allows the formation of ferroelastic domains, whose ferroelectric nature is debated [19,20]. Ferroelastic and ferroelectric materials show nanoscale domains with different crystal orientation. These domains can present lattice tilt relative to each other, due to lattice mismatch at domain boundaries. In oxide perovskites, such domains have been studied for years [21,22], and their response to heating [23] and external electrical and mechanical excitation [24] is known. Recently, the existence of ferroelastic domains in MHPs [25–28], as well as their impact on the basic materials properties [29,30], has been shown. It is still an open question, however, how these domains form and evolve during crystal phase transitions, as the lattice symmetry is changed. In particular, the timescale of the domain formation is unclear, and whether the entire crystal changes simultaneously or presents local variations due to strain inhomogeneities or crystal defects [14,16]. Furthermore, it is unknown whether the domains change deterministically and reversibly upon repeated transitions, and if the process is symmetric when changing from lower to higher crystal symmetry, and vice versa.

These questions are challenging to study experimentally, as they require a method able to probe quite large crystals with good spatial and time resolution. It is common to use indirect

*lucas.marcal@sljus.lu.se

methods such as microphotoluminescence [4,31,32], which has a spatial resolution of about half a micron. Transmission electron microscopy (TEM) and scanning probe microscopy (SPM) have much better spatial resolution and have been used to image MHP domains [33,34], but struggle to study extended objects. Recently, we used scanning nanofocused x-ray diffraction (nano-XRD) to follow the domain dynamics of $CsPbBr_3$ nanowires, combining high spatial resolution and large field of view with excellent sensitivity to lattice strain and tilt [26]. Mapping large structures using nano-XRD, however, takes tens of minutes. Furthermore, the absorbed x-ray dose is very high and eventually leads to structural damage, even in the relatively radiation-stable $CsPbBr_3$.

Here, we show that these challenges can be overcome by applying the recently developed full-field diffraction x-ray microscopy (FFDXM) method to image nanoscale crystal domains in single crystal $CsPbBr_3$ nanoplatelets. FFDXM illuminates the sample using a quite large x-ray beam, typically tens of microns, and a set of compound refractive lenses (CRLs) to select a desirable Bragg condition to project a magnified real-space image of the sample on the x-ray detector [35,36]. This technique allows the study of local strain and lattice tilt of extended objects with spatial resolution on the order of 100 nm and time resolution of a few seconds. FFDXM has previously been demonstrated for static imaging [37,38], but the fast acquisition makes it ideally suited for *in situ* and *in operando* experiments. We observe local changes in the nanoscale domains that are sometimes faster than the 6 s time resolution, and distinct high-temperature and low-temperature domain patterns. The low-dose acquisition allows us to perform multiple heating and cooling cycles, which reveals that we can reversibly switch between the two patterns.

II. EXPERIMENT

A. Growth

$CsPbBr_3$ nanoplatelets or nanowires were grown on a fused silica glass substrate by thermal evaporation at elevated temperatures $>360\,^{\circ}C$, analogously to previous reports [39–41]. For the experiment described here, the nanoplatelets were deposited on an amorphous substrate instead of single crystal sapphire [39] or mica [40,41]. The noncatalyzed growth was carried out in a three-zone horizontal-tube furnace. The quartz tube reactor was purged with a N_2 (99.999%, Gordon Gas) and H_2 (99.99995%, Parker Dominic Hunter H_2-generator) 7:1 mixture and maintained at 300 mbar with a constant 400 SCCM (cubic centimeter per minute at STP) flow of the N_2/H_2 mixture during the growth process. For the growth process, 150–180 μm thick, UV-grade, fused silica glass (Laser Optex Inc.) substrates were used. CsBr and $PbBr_2$ powders (both purchased from Sigma-Aldrich) were mixed in a 1:2 molar ratio and heated at 390 °C for 20 min in the same N_2/H_2 atmosphere to generate the precursor. During the growth process the precursor was held at 550 °C in the first heating zone of the furnace, while the silica glass samples were placed downstream in the second heating zone and held at 360 °C. After a 15 min growth period, the furnace was moved away, and the source and sample could be rapidly cooled down to room temperature.

B. Structural characterization

We used FFDXM to study the crystal evolution of a single nanoplatelet, 15.9 μm long and 2.8 μm wide, during temperature variation, as shown in the schematic in Fig. 1(a). Without further preparation, the sample was mounted onto a heating stage and aligned in the x-ray focus, with its long axis horizontally aligned in the laboratory reference. The FFDXM experiment was performed in transmission geometry at the ID01 beamline, at the European Synchrotron Radiation Facility (ESRF), in Grenoble, France [42]. The beam was focused to 70×70 μm² (vertical×horizontal) spot size using a double-reflection monochromator at 34 m from the source, allowing imaging of the whole nanoplatelet in a single frame. The energy of the beam was fixed at 9.0 keV (wavelength 1.3776 Å) during the full-field diffraction experiments, with an incident flux of 10^{12} photons/s, reduced to 10^{10} photons/s using absorbers. Be compound refractive lenses (CRLs) with 119.5 mm focal length and 115 mm entrance aperture were subsequently used to image the diffracting regions on an Andor Zyla 5.5 sCMOS camera with 2560×2160 pixels (6.5 μm pixel size), installed in a vacuum pipe. The detector was positioned 6.5 m from the sample, giving a magnification ratio of 65:1 and setting the effective pixel size to 100 nm. The CRLs have an effective aperture of 230 μm and were positioned 100 mm from the sample. The sample was mounted inside a furnace, which allowed for temperature variation. The temperature was monitored and regulated by a thermocouple placed within an alumina holder, where the sample was mounted. Both the holder and the heater were in alumina, and two stainless steel screws were holding the alumina plates together to clamp the sample. It was designed so the sample was in transmission geometry. The heater controller was integrated to the beamline control system, so it was possible to change the sample temperature without the need to enter the hutch. Temperature at the sample was recorded every 1 s during the experiment. The furnace was placed on a PI-Mars three-axis piezo on top of a BORA hexapod with three axes of translation with right-handed rotation for each axis.

The set of lenses was positioned after the sample at $2\theta = 27.17^\circ$ to collect the $CsPbBr_3$ orthorhombic *Pbnm* 004 Bragg reflection and project a real-space image of the nanoplatelet, 65 times magnified, on the x-ray detector. The heating chamber with the sample orientation was set to match the conditions for the orthorhombic 004 Bragg condition. Scanning electron microscopy (SEM) was used to retrieve the nanoplatelet morphology, depicted in the inset. Note that the right part of the nanoplatelet bends 4° in the substrate plane relative to its left part, tilting the crystal structure out of the lenses' acceptance range. Each pixel on the maps corresponds to 100 nm, but the imaging resolution is about 150 nm [35].

III. RESULTS

A. Domain dynamics during heating

The signal in FFDXM is selected in two stages. First, only the parts of the sample that have the correct orientation for the Bragg condition will contribute to diffraction. This condition can be tuned by rotating θ, which allows the visualization of domains presenting different tilt along the Bragg angle.
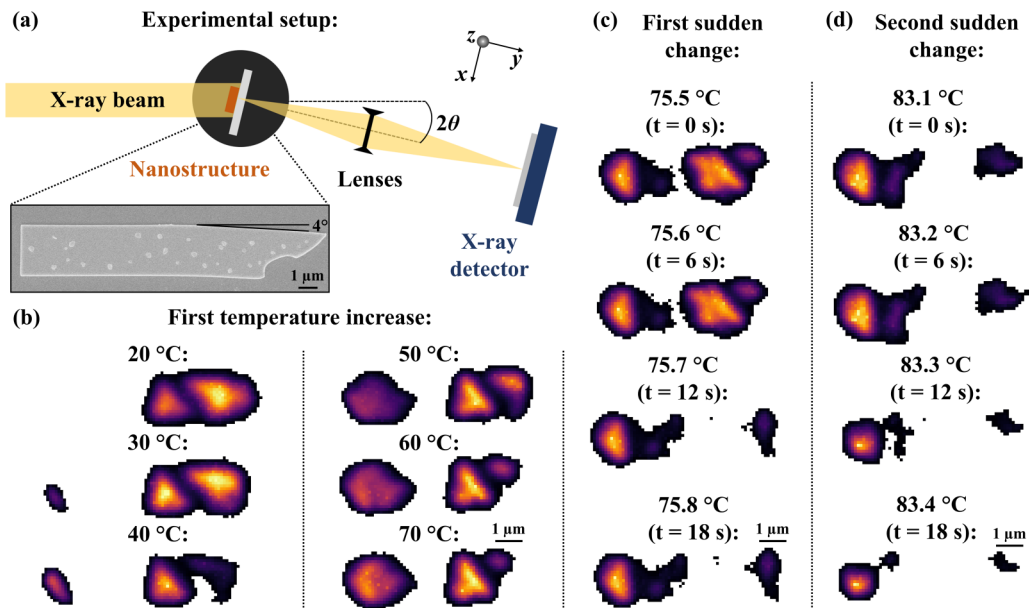
FIG. 1. (a) Schematic representation of the FFDXM experimental setup. The nanoplatelet was rotated to the Bragg angle θ, and the x-ray detector was positioned at 2θ. The bright areas are domains with both lattice tilts aligned by the rotation motor as well as lattice spacing within the 2θ condition selected by the lenses. The lenses create a 65 times magnified image of the bright parts of the nanoplatelet on the detector. Inset shows a SEM image of the nanoplatelet, acquired after the experiment. The right part of the structure bends $4°$ relative to its left part, tilting the crystal out of the lenses' acceptance range. (b) Projections at a specific θ of the nanoplatelet acquired at temperatures ranging from $20°C$ to $70°C$ during temperature increase. (c) Images near $75.7°C$, evidencing a sudden change in the domain orientation pattern in the central part. (d) Images near $83.3°C$, showing another sudden change in the left part of the nanoplatelet. Note the marginal differences between the last frame in (c) and the first two frames in (d), despite the large temperature change. Subsequent frames in (c),(d) were acquired with a time difference on the order of 6 s. Movies showing the changes represented in (c),(d) can be found in the Supplemental Material [43].

Second, only a small range of diffraction is selected by the lens aperture. With an effective aperture of 230 μm, mounted 100 mm from the sample, the lenses were able to collect diffracted photons in a range of $0.13°$ [42]. This criterion can be changed by rotating the lenses and the x-ray detector along 2θ; however, it was left constant at $27.17°$ for all the experiments shown here [35]. The only exception was in the first temperature cycle, where minor optics realignments were made as described in detail in Table 1 in the Supplemental Material [43]. It is important to notice that lattice tilt along α, defined as the rotation around y, would only be visible by rotating the sample and detector around the optical axis, not accessible in this experiment, and thus the $4°$ tilted part of the nanoplatelet is not visible in our measurements. To achieve the best possible time resolution over temperature variation, the incident θ angle was fixed during heating while single projections were collected (again, with a few minor exceptions in the first cycle). Frames were acquired every 6 s, limited by the detector readout time, which is about 100 times faster than our previous scanning nano-XRD report [26]. The rate corresponds to an increase of about $0.1°C$ per projection. Here we show only a selection of the most interesting projections, while the full cycle is shown as movies in the Supplemental Material [43]. Table 1 [43] lists all the movies. At certain points, the temperature was held constant while a rocking curve (θ scan) was collected, but these results are discussed further below.

At $20°C$, two domains interfacing each other along a diagonal domain wall were observed, as depicted in the top panel of Fig. 1(b). It has been reported in the literature that *Pbnm* (112) planes are possible domain walls for different orthorhombic $CsPbBr_3$ thin films [25], nanowires [27] and nanoparticles [44], which justifies the interest on tracking the evolution of this area. As the temperature was increased, the gradual growth of a new domain on the left part of the nanoplatelet could be seen. It is notable that, as the left domain became more visible at higher temperatures, two diagonal shaped domain walls on its right side emerged. At higher temperatures, one of the two initially visible domains on the right part faded away. The triangular shaped domain near the center of the nanoplatelet, however, did not change significantly in this temperature range, preserving its shape and size. These gradual changes could be related to thermal expansion of the lattice.

We continued to ramp the temperature until $90°C$, above the orthorhombic to tetragonal phase transition in bulk $CsPbBr_3$ [13]. Unlikely the gradual variations seen at lower temperatures, a few sudden changes were noted in this temperature range. A large domain near the center disappeared at $75.7°C$, as depicted in Fig. 1(c). A new striped domain also appeared on the right side of the nanoplatelet at the same time. The changes were fast enough to be seen in two subsequent frames, showing that the whole process occurred in less than 6 s and possibly much faster. Another significant change in the nanoplatelet structure was also noted near $83.3°C$, when both the left and right domains waned in three subsequent frames, as depicted in Fig. 1(d). Note the marginal differences between the last frame in Fig. 1(c) and the first two frames

(a)   **First temperature decrease:**

(b)   **Sudden change during second
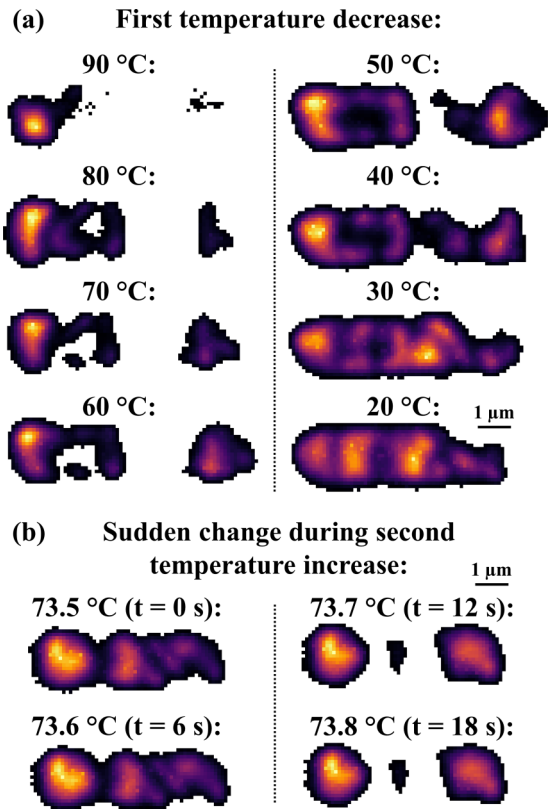temperature increase:**

FIG. 2. (a) Projections of the nanoplatelet acquired during first cooldown. (b) Projections near 73.7 °C, acquired during second heating cycle, showing a sudden and localized change in the domain pattern. Frames were acquired with a time difference on the order of 6 s.

in Fig. 1(d), despite the large temperature shift. All domain changes can be seen in the movies and are listed in Table 1, in the Supplemental Material [43]. Similar processes have been reported near 80 °C for CsPbBr$_3$ nanowires using scanning XRD [26]. That technique, however, presents relatively poor time resolution and was unable to show the fast and local behavior of the changes.

B. Cooling and second heating cycle

In order to check the stability and reversibility of the new domain configuration seen at high temperatures, the sample was cooled down to 20 °C, as shown in Fig. 2(a). Unlike the heating cycle, however, no sudden changes were noted close to the phase-transition temperature in the cooling process, just gradual domain reallocations. Instead, a few sudden changes were noted at much lower temperature, below 40 °C, which reveals an asymmetry and hysteresis in the process. Structural hysteresis has been observed for CsPbBr$_3$ nanowires using nano-XRD, when domains formed during the orthorhombic to tetragonal phase transition had their shape partially preserved at lower temperatures during cooling down [26]. Thermal hysteresis has also been reported for different types of perovskites [45,46], including CsPbBr$_3$ [47]. Haque and Mativenga suggest for the lead halide perovskite MAPbI$_3$ that the polarization effect of the cation is responsible for the hysteresis in the orthorhombic regime, while in the tetragonal phase it is associated with ion migration [48]. Although we only have access to a small portion of the reciprocal space via FFDXM, the gradual, rather than drastic, domain rearrangement arising from structural hysteresis is expected to produce the same effects observed here and plotted in Fig. 2(a).

As the temperature decreased toward 50 °C, both the left and right visible domains grew and became more intense, and from 50 °C to 20 °C, the newly formed right one gradually faded away. The formerly blank area in the central right region became visible, evidencing a diagonal domain wall at the same position as was seen before the heating cycle, in Fig. 1(b).

To investigate the reproducibility of the domain dynamics, a second heating cycle up to 80 °C was performed. Unfortunately, the sudden change at 83.3 °C during the first heating was only noted after the experiment, and we only heated the nanoplatelet to 80 °C in subsequent cycles. Again, gradual variations were seen for the temperature range between 20 °C and 70 °C. A sudden change in the domain configuration took place near 73.7 °C, similar in both morphology and temperature to the change at 75.7 °C observed in the first cycle, as depicted in Fig. 2(b). A triangular structure can be seen initially, similar to Fig. 1(b), as well as a diagonal domain wall on its right side. After the sudden change, however, both features disappeared, and only three separate domains were visible along the nanoplatelet. Note that only certain domains are visible at a specific incidence angle, and with a different θ we would see other domains and probably other sudden changes. In this experiment, we focused on the reproducibility of the domain patterns by keeping θ nominally constant.

C. Repeated temperature cycles and rocking curves

Subsequently, we cooled and heated the nanoplatelet two more cycles. At selected points, the temperature was held constant while performing a rocking curve, i.e., a θ scan. Figure 3(a) shows the integrated intensity (left column), crystal lattice tilt (middle column), and rocking curve broadening (right column) maps at selected temperatures. The latter was retrieved from the full width at half maximum (FWHM) of the rocking curve, point by point along the nanoplatelet. Since the peak width increases in areas with large tilt variations, this signal is especially useful to visualize domain walls. An overview of the entire temperature cycle of our experiment is shown in Fig. 3(b), with the scan number corresponding to each rocking curve. Note that the time-temperature profile represents the four complete heating cycles of the experiment and includes data from Figs. 1 and 2. For instance, the first heating ramp present in Fig. 1 corresponds to frames acquired between rocking curves 1 and 3; the first cooling down shown in Fig. 2(a) occurs between 2 and 4; and frames of Fig. 2(b), which correspond to the second heating cycle, were acquired between 5 and 6. Figures 3(c) and 3(d) show the total diffracted intensity as a function of θ for the rocking curves at 20 °C and 80 °C, respectively.

The upper panel of Fig. 3(a) shows rocking curve 1, performed with the pristine nanoplatelet before the first heating cycle, at 20 °C. The lattice tilt map shows an internal variation on the order of 0.04 ° along θ, with abrupt changes near the domain walls. The lack of blank areas in the intensity image at 20 °C, aside from the diagonal feature, evidence that
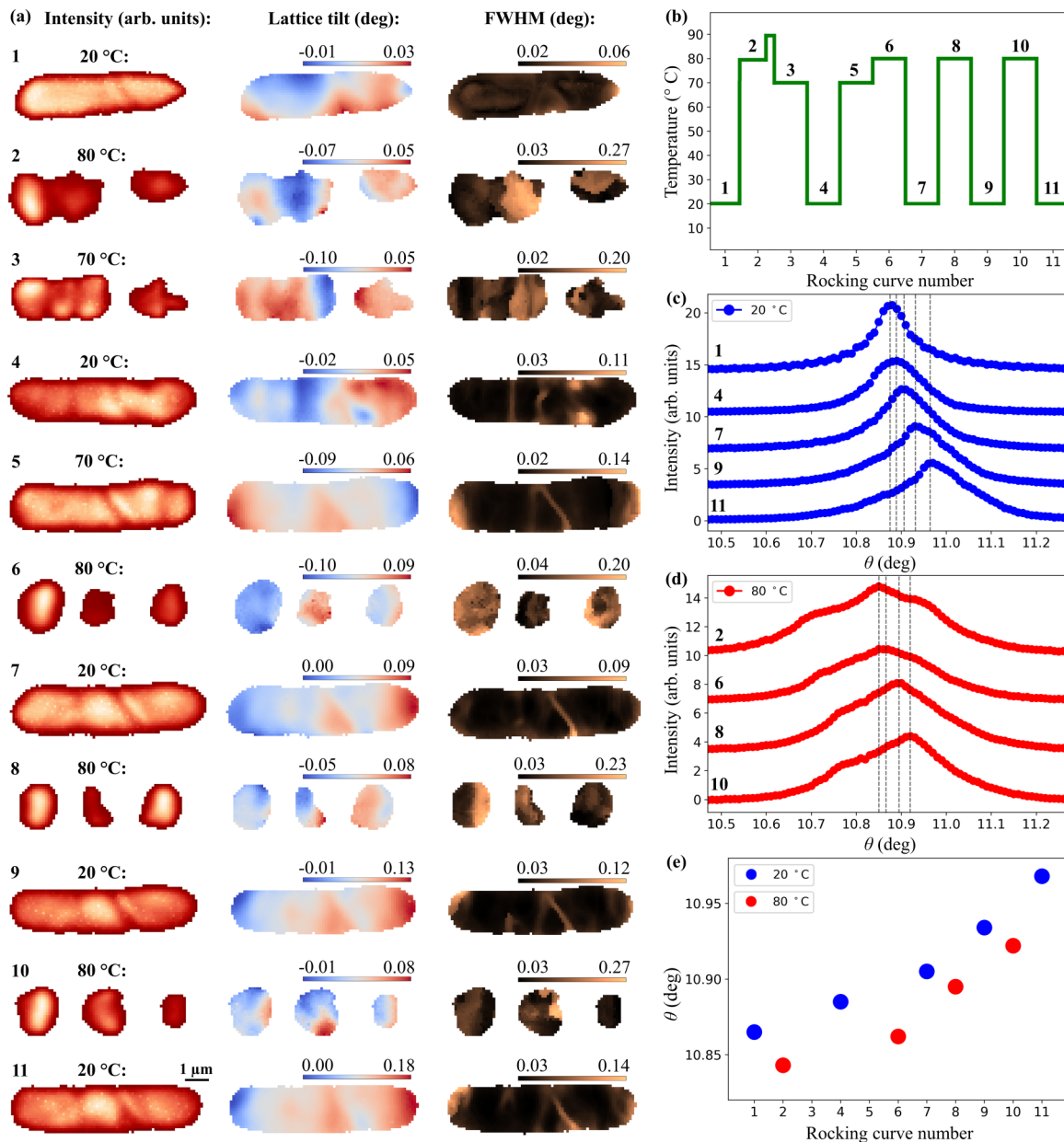
FIG. 3. (a) Maps of the integrated intensity (left panels), lattice tilt (middle panels), and peak width measured as FWHM (right panels), of the nanoplatelet at selected temperatures along the heating cycles. The maps are stacked from top to bottom following the chronological order. Note that the range of the color scale is adapted for each map, for better visualization of local features. (b) Schematic graph of the full temperature cycle. Numbers from 1 to 11 indicate where rocking curves were acquired and correspond to the maps plotted in (a). Fast single-frame measurements as in Figs. 1 and 2 were performed during the changes in temperature, between the rocking curves. (c),(d) Diffracted intensity as a function of the incident angle θ plotted for the rocking curves at 20 °C and 80 °C, respectively. Curves are stacked from top to bottom in chronological order and numbers correspond to the maps in (a). The θ values were retrieved from the nominal motor position and do not correspond to the exact sample rotation with respect to the x-ray beam. (e) Plot showing the θ peak position for each map at both 20 °C and 80 °C, as marked in (c),(d) by the black dashed lines.

inhomogeneities observed in single projections, e.g., Fig. 1(b), are due to local crystal tilts along θ. Large variations in lattice spacing, i.e., 2θ, would in contrast give scattering outside of the lenses' acceptance angle. Also, domain walls oriented as the diagonal stripe could give rise to lattice tilt around the optical axis [26], which is inaccessible without moving the detector.

A second rocking curve (map 2) was acquired after reaching 80 °C. Unlike map 1, the rocking curve at this temperature

shows blank areas, indicating that part of the nanoplatelet either presents a different crystal phase or its crystal structure is rotated around the optical axis. The temperature was then increased until 90 °C and subsequently cooled down back to 20 °C. Two rocking curves were acquired along the first cooling down, at 70 °C and 20 °C. Maps are stacked below the first 80 °C map and indexed as 3 and 4, respectively. Although no obvious pattern shows up at the highest temperature, a tilted striped domain can be seen in blue in the 70 °C tilt
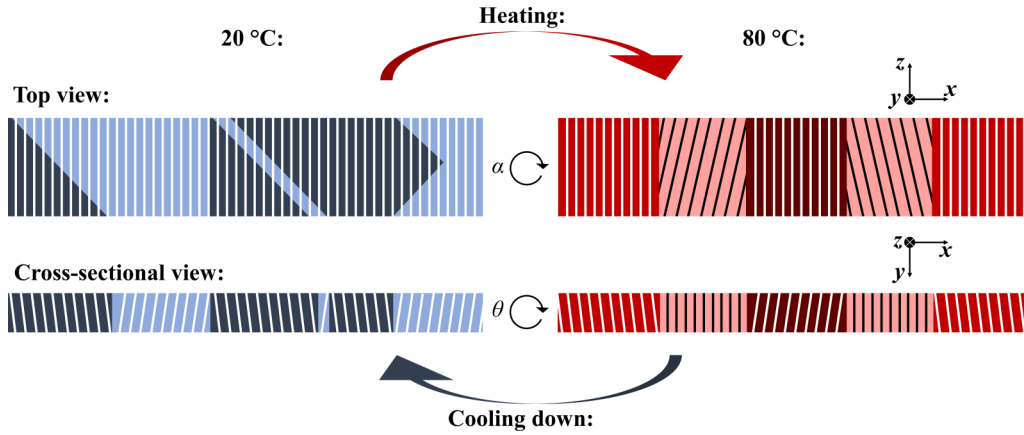
FIG. 4. Sketch showing the top and cross-sectional view of the nanoplatelet at 20 °C (blue) and 80 °C (red). Different color tones represent domains along the structure. White lines indicate the orientation of orthorhombic or tetragonal (001) planes, evidencing the tilts along θ and α in multiple domains at both temperatures. Black lines indicate tetragonal (110) planes at 80 °, which are invisible since their 2θ is out of the acceptance range of the imaging lenses.

map. As the temperature is reduced to 20 °C, the intensity inhomogeneities are less pronounced and map 4, albeit not identical to map 1, is overall smoother than the high-temperature ones. The diagonal line separating domains on the right side of the nanoplatelet also became visible again in map 4.

During the second heating cycle, rocking curves were performed at both 70 °C (map 5), before the sudden change, and at 80 °C (map 6). Note that while the first 70 °C map, 3, was acquired during a cooling cycle, the second one (5) was acquired during a heating cycle. The intensity map, 5, shows no significant local inhomogeneities, presenting an overall shape, including the diagonal line, similar to 20 °C (map 4). The lattice tilt map, however, has a larger variation range and presents areas with opposite tilt values when compared to its low-temperature counterpart. At 80 °C not all of the nanoplatelet was visible along the rocking angle anymore, but instead three domains emerged. In general, regions with abrupt lattice tilt variations along the crystal will present broader rocking curves. It is notable that the FWHM maps at 80 °C present larger scale range, when compared with low-temperature ones, indicating higher local disorder.

D. Reproducibility of low- and high-temperature patterns

All 20 °C maps present similarities, without blank regions along the structure, a pronounced diagonal domain wall in the central right part, and an overall positive lattice tilt gradient from left to right along the nanoplatelet. Differences in the diffraction area from the first 20 °C map to the subsequent ones suggest possible strain relaxation at the buried substrate interface after slower cooldown from 90 °C, relative to the fast cooldown by removing the furnace after growth. Such hypothesis is corroborated by the lack of substantial differences between the second, third, and fourth low-temperature rocking curves. Likewise, the 80 °C maps are similar, with three well defined domains and blank areas in between. A schematic representation of domains and crystallographic planes at both low and high temperatures is depicted in Fig. 4. The left panels in blue represent a nanoplatelet at 20 °C, while the right panels

in red represent the structure at 80 °C. In both cases, multiple color tones indicate different domains, while the crystal plane orientation is depicted by white and black bars. Note that the planes' inclination in the cross-sectional view indicates lattice tilt along the rocking angle θ, while in the top view it indicates tilts along α, which would lead to blank domains in our measurements.

The θ for the maxima of the 80 °C peaks are consistently lower than for the 20 °C map ones. This can be observed when the central peak position for each rocking curve at both 20 °C (blue dots) and 80 °C (red dots) is plotted as in Fig. 3(e). We also note that the peaks gradually shift toward higher θ angles after each cycle. Since the lenses and detector were held at the same 2θ, this is not due to changes in the crystal structure but likely small creep of the sample or the rotation stage. In addition, we note that the peaks at 80 °C, as in Fig. 3(d), are generally much broader than the ones at 20 °C, depicted in Fig. 3(c). The 80 °C peaks have a shoulder between 10.7 ° and 10.8 °, and a second shoulder is also visible in curve 2 near 10.950 °. This is an effect caused by the tilted domains seen at the high-temperature maps in Fig. 3(a), unlike the smooth variations in the 20 °C maps. To quantify the shift in peak position, we calculated the difference between the 80 °C peak positions and their previous and subsequent 20 °C peaks, finding an average value of $\Delta\theta = 0.03°$. One can also notice a systematic clenching of the rocking curves at high temperature with subsequent cycles, indicating a sharper lattice tilt distribution profile within visible domains at 80 °C, which has already been indicated on the maps shown in Fig. 3(a). It might be expected that rocking curve 2 can be different from the other ones, since the nanoplatelet was heated up from its initial stage, before strain relaxation of subsequent cycles. Curves 8 and 10 are very similar, but significantly different from 6. It is important to notice, however, that we have performed a rocking scan at 70 °C before curve 6 acquisition, which significantly increased the total time spent in this cycle, compared to the next two. A less pronounced opposite effect can be seen at low temperature, with a broadening of the rocking curves from curves 1–4, 7, and 9. Again, 1 was acquired before the heating cycles and strain relaxation, and

its comparison with subsequent ones is complex. A scan corresponding to 4 was performed after a cycle up to 90 °C, also different from the others, when domain configuration may be different from the 80 °C. The lower time spent at higher temperatures before curve 9, when compared to 7, can also be responsible for differences in the nanoplatelet bending seen between these two cases.

E. Crystal structure evolution

We first discuss the crystal structure at low temperature, and then the high-temperature results. At room temperature, we observe domains that appear at different θ angles. We determined the positions of the 004 and 220 orthorhombic Bragg peaks by measuring different parts of the sample without using the lenses, as shown in the Supplemental Material [43], and measuring CsPbBr$_3$ nano-objects with domains in both orientations, as in previous reports [27,44]. By comparing with the observed Bragg peak of the nanoplatelet, we find that the detected peak corresponds to the orthorhombic 004 Bragg reflection. The 2θ position corresponds to a compressive strain on the order of 0.3% compared to bulk CsPbBr$_3$ [13]. The nanoplatelet has the c axis along its long axis, so the whole structure presents (001) planes orthogonal to the nanoplatelet axis at 20 °C, in accordance with previous works on CsPbBr$_3$ nanowires [26,27], and the domains only differ in lattice tilt at this temperature. At the domain walls, the lattice mismatches of a to b will lead to lattice tilts, as previously described for different structures [25,27], which means the domains will have different tilts around θ and α. They represent the four possible different rotations around the c axis, with the a axis parallel or orthogonal to the substrate plane. Previous works report lattice tilts around 0.4 ° in each direction, on similar structures at higher temperatures in the tetragonal regime [26]. Using a similar approach, one can expect to find, for orthorhombic CsPbBr$_3$, lattice tilt variations up to $\omega = 1-(a/b) = 0.33°$. With the present spatial resolution, however, the tilt is averaged in an area of approximately 150 nm, and the magnitude of the tilt is attenuated. All 20 °C maps systematically show both orthogonal and diagonal domain walls. Orthogonal ones might correspond to (001) planes, in accordance with the previously determined position of the Bragg peak. The diagonal ones, however, cannot be directly determined without rotating the nanoplatelet around the optical axis, but one hypothesis is that they correspond to (112) planes, in agreement with previous reports for CsPbBr$_3$ films [25] and nanowires [27]. This crystal orientation would have {110}-type planes orthogonal to both nanoplatelet short axes. A much simpler domain pattern is visible in the 80 °C maps, with domain walls aligned perpendicular or parallel with the nanoplatelet long axis. This is expected for the higher-symmetry tetragonal phase and is in line with our recent nano-XRD imaging of a similar structure [26].

As the temperature was increased, we observe that the domain pattern changes, where some domains suddenly became invisible, and others remained visible with the same shape. A transition from orthorhombic to the higher-symmetry tetragonal crystal phase is expected near 80 °C [13,26], and the most straightforward explanation for the sudden changes is therefore that they are related to this phase transition. The

tetragonal crystal structure would allow either the (001)- or one of the four {110}-type planes to be orthogonal to the nanoplatelet long axis. The tetragonal 002 Bragg peak is only 0.07 ° below the orthorhombic 004 peak in 2θ, well within the acceptance range of the imaging lenses, so tetragonal domains with (001) planes orthogonal to the nanoplatelet axis can still be visible for the set 2θ position. The peak shift plotted in Fig. 3(e), found to be $\Delta\theta = 0.03°$, as discussed above, is about half the expected 2θ split [13], which corroborates this hypothesis. However, this shift could also be related to thermal expansion of the sample and the substrate. In contrast, the tetragonal 220 Bragg peak should not be visible since it is 0.18 ° above the 004 orthorhombic. This is an indication that regions invisible at any θ in Fig. 3 must represent one of the four {110}-type tetragonal domains with the c axis orthogonal to the long axis of the nanoplatelet, while the visible domains present (001) planes along the nanoplatelet axis. The hypothesis of intercalated 001- and 110-type domains near the orthorhombic to tetragonal transition temperature is also consistent with a previous report on CsPbBr$_3$ nanowire [26]. A schematic representation of both orthorhombic and tetragonal planes can be seen in the Supplemental Material (Fig. S2) [43].

Thus, the remaining visible domains could be either tetragonal or orthorhombic 001-type domains, which leads to two scenarios. In the first one, the domains that remain visible, for instance, the leftmost domain in Fig. 1(c), do undergo a simultaneous tetragonal phase transition near 75 °C but keep exactly the same domain shape in the process. That is, the ferroelastic domain shapes in the orthorhombic crystal are transferred to the tetragonal crystal structure. This scenario is difficult but not impossible to reconcile with the observation of multiple sudden change at other temperatures and times, such as at 83.3 °C in Fig. 1(d), which would then require a ferroelastic domain rearrangement within a fully tetragonal crystal. The second scenario is that some of the visible domains still have an orthorhombic structure, and intermediate states of the nanoplatelet represent a mix of orthorhombic and tetragonal domains. Indeed, dual phase coexistence has been previously reported for MHPs [4,49], and the orthorhombic peak would be well within the high-temperature peak width of the rocking curve in Fig. 3(d).

IV. CONCLUSION

In conclusion, we have shown that *in situ* FFDXM can be used to study the formation and dynamics of nanoscale domains with high spatial and temporal resolution. Our results elucidate the dynamics of domains in MHPs and describe details of their basic structural properties. We want to highlight two unexpected results. First, we find that the pattern changes at distinct temperatures in different domains. The two sudden changes near 75.7 °C and 83.3 °C depicted in Figs. 1(c) and 1(d) evidence the local behavior of the phase transition captured by the fast imaging. One possible reason is that defects lead to local fluctuations in the transition temperature [17]. A previous report showing domain formation during phase transition was unable to visualize local sudden changes [26], which is only possible using a technique able to combine both high spatial and temporal resolution, such as FFDXM. The

second key result is the similarities in all 20 °C, as well as in all 80 °C maps, evidencing a reproducibility of the domain formation over multiple cycles. In particular, the diagonal feature appears in all low-temperature maps, but none of the high-temperature ones, while the three-domain pattern appears in all high-temperature maps. The determination of the crystal orientation at both low and high temperatures helped to understand the nature of the sudden changes seen during heating. Clearly, the domain patterns are not formed randomly. We speculate that defects could also be responsible for the reproducible domain patterns at both low and high temperature, in addition to the local variations discussed above.

The imaging of the domain patterns over repeated temperature cycles was made possible not only by the high speed, but also by the relatively low x-ray dose of FFDXM. In this particular case, the absorbed dose of a single angle projection was reduced about three orders of magnitude, from $D = 2.1 \times 10^8$ Gy at a previous nano-XRD experiment [26] to about $D = 5.4 \times 10^4$ Gy using FFDXM. The number of temperature cycles here was limited by the available time, not by beam damage.

Although the temporal resolution here is already impressive, it should be possible to improve substantially. We used 1 s integration time and 5 s readout, and the latter could be reduced to the millisecond range with better readout routines. Faster measurements could allow many more temperature

cycles within an experiment. More generally, the experiment demonstrates how the developed FFDXM technique is uniquely suited to study local domain evolution in ferroic materials with excellent spatial and temporal resolution, allowing for *in situ* and *in operando* investigations. Similar experiments could be used to study fast domain dynamics in a wide range of ferroic systems, also with electrical or optical stimulation.

[1] W. Zhang, G. E. Eperon, and H. J. Snaith, Nat. Energy **1**, 16048 (2016).

[2] T. A. S. Doherty, A. J. Winchester, S. Macpherson, D. N. Johnstone, V. Pareek, E. M. Tennyson, S. Kosar, F. U. Kosasih, M. Anaya, M. Abdi-Jalebi, Z. Andaji-Garmaroudi, E. L. Wong, J. Madeo, Y. H. Chiang, J. S. Park, Y. K. Jung, C. E. Petoukhoff, G. Divitini, M. K. L. Man, C. Ducati *et al.*, Nature (London) **580**, 360 (2020).

[3] M. R. Filip, G. E. Eperon, H. J. Snaith, and F. Giustino, Nat. Commun. **5**, 5757 (2014).

[4] A. Dobrovolsky, A. Merdasa, E. L. Unger, A. Yartsev, and I. G. Scheblykin, Nat. Commun. **8**, 34 (2017).

[5] E. Oksenberg, E. Sanders, R. Popovitz-Biro, L. Houben, and E. Joselevich, Nano Lett. **18**, 424 (2018).

[6] M. V. Kovalenko, L. Protesescu, and M. I. Bodnarchuk, Science **358**, 745 (2017).

[7] M. S. Kirschner, B. T. Diroll, P. Guo, S. M. Harvey, W. Helweh, N. C. Flanders, A. Brumberg, N. E. Watkins, A. A. Leonard, A. M. Evans, M. R. Wasielewski, W. R. Dichtel, X. Zhang, L. X. Chen, and R. D. Schaller, Nat. Commun. **10**, 504 (2019).

[8] J. Shamsi, A. S. Urban, M. Imran, L. De Trizio, and L. Manna, Chem. Rev. **119**, 3296 (2019).

[9] J.-K. Chen, Q. Zhao, N. Shirahata, J. Yin, O. M. Bakr, O. F. Mohammed, and H.-T. Sun, ACS Mater. Lett. **3**, 845 (2021).

[10] Y. Nagaoka, K. Hills-Kimball, R. Tan, R. Li, Z. Wang, and O. Chen, Adv. Mater. **29**, 1606666 (2017).

[11] S. Yesudhas, M. V. Morrell, M. J. Anderson, C. A. Ullrich, C. Kenney-Benson, Y. Xing, and S. Guha, Chem. Mater. **32**, 785 (2019).

[12] H. Zhang, F. Wang, Y. Lu, Q. Sun, Y. Xu, B.-B. Zhang, W. Jie, and M. G. Kanatzidis, J. Mater. Chem. C **8**, 1248 (2020).

[13] C. C. Stoumpos, C. D. Malliakas, J. A. Peters, Z. Liu, M. Sebastian, J. Im, T. C. Chasapis, A. C. Wibowo, D. Y. Chung, A. J. Freeman, B. W. Wessels, and M. G. Kanatzidis, Cryst. Growth Des. **13**, 2722 (2013).

[14] P. Cottingham and R. L. Brutchey, Chem. Mater. **30**, 6711 (2018).

[15] F. Bertolotti, L. Protesescu, M. V. Kovalenko, S. Yakunin, A. Cervellino, S. J. L. Billinge, M. W. Terban, J. S. Pedersen, N. Masciocchi, and A. Guagliardi, ACS Nano **11**, 3819 (2017).

[16] J. A. Steele, H. Jin, I. Dovgaliuk, R. F. Berger, T. Braeckevelt, H. Yuan, C. Martin, E. Solano, K. Lejaeghere, S. M. J. Rogge *et al.*, Science **365**, 679 (2019).

[17] J.-P. Ma, J. Yin, Y.-M. Chen, Q. Zhao, Y. Zhou, H. Li, Y. Kuroiwa, C. Moriyoshi, Z.-Y. Li, O. M. Bakr, O. F. Mohammed, and H.-T. Sun, ACS Mater. Lett. **1**, 185 (2019).

[18] F. Bertolotti, G. Nedelcu, A. Vivani, A. Cervellino, N. Masciocchi, A. Guagliardi, and M. V. Kovalenko, ACS Nano **13**, 14294 (2019).

[19] E. Strelcov, Q. Dong, T. Li, J. Chae, Y. Shao, Y. Deng, A. Gruverman, J. Huang, and A. Centrone, Sci. Adv. **3**, 8 (2017).

[20] H. Rohm, T. Leonhard, A. D. Schulz, S. Wagner, M. J. Hoffmann, and A. Colsmann, Adv. Mater. **31**, 1806661 (2019).

[21] P. R. Potnis, N. T. Tsou, and J. E. Huber, Materials (Basel) **4**, 417 (2011).

[22] K. T. Kang, H. I. Seo, O. Kwon, K. Lee, J.-S. Bae, M.-W. Chu, S. C. Chae, Y. Kim, and W. S. Choi, Appl. Surf. Sci. **499**, 143930 (2020).

[23] J. Diao, X. Shi, T. A. Assefa, L. Wu, A. F. Suzana, D. S. Nunes, D. Batey, S. Cipiccia, C. Rau, R. J. Harder, W. Cha, and I. K. Robinson, Phys. Rev. Materials **4**, 106001 (2020).

[24] P. Gao, J. Britson, C. T. Nelson, J. R. Jokisaari, C. Duan, M. Trassin, S. H. Baek, H. Guo, L. Li, Y. Wang, Y. H. Chu, A. M. Minor, C. B. Eom, R. Ramesh, L. Q. Chen, and X. Pan, Nat. Commun. **5**, 3801 (2014).

[25] X. Zhang, F. Wang, B.-B. Zhang, G. Zha, and W. Jie, Cryst. Growth Des. **20**, 4585 (2020).

[26] L. A. B. Marcal, E. Oksenberg, D. Dzhigaev, S. Hammarberg, A. Rothman, A. Bjorling, E. Unger, A. Mikkelsen, E. Joselevich, and J. Wallentin, ACS Nano **14**, 15973 (2020).

[27] L. A. B. Marçal, S. Benter, A. Irish, D. Dzhigaev, E. Oksenberg, A. Rothman, E. Sanders, S. Hammarberg, Z. Zhang, S. Sala, A. Björling, E. Unger, A. Mikkelsen, E. Joselevich, R. Timm, and J. Wallentin, Phys. Rev. Materials **5**, L063001 (2021).

[28] V. L. R. Jacques, A. Gallo-Frantz, A. Tejeda, D. Le Bolloc'h, F. Lédée, G. Trippé-Allard, D. Garrot, P. Fertey, E. Deleporte, and O. Plantevin, J. Phys. D: Appl. Phys. **52**, 314001 (2019).

[29] X. Xiao, W. Li, Y. Fang, Y. Liu, Y. Shao, S. Yang, J. Zhao, X. Dai, R. Zia, and J. Huang, Nat. Commun. **11**, 2215 (2020).

[30] R. Shi, Z. Zhang, W. H. Fang, and R. Long, Nanoscale Horiz. **5**, 683 (2020).

[31] N. A. Gibson, B. A. Koscher, A. P. Alivisatos, and S. R. Leone, J. Phys. Chem. C **122**, 12106 (2018).

[32] S. M. Lee, C. J. Moon, H. Lim, Y. Lee, M. Y. Choi, and J. Bang, J. Phys. Chem. C **121**, 26054 (2017).

[33] W. Li, Z. Zhang, E. G. Bithell, A. S. Batsanov, P. T. Barton, P. J. Saines, P. Jain, C. J. Howard, M. A. Carpenter, and A. K. Cheetham, Acta Mater. **61**, 4928 (2013).

[34] X. Li, S. Chen, P. F. Liu, Y. Zhang, Y. Chen, H. L. Wang, H. Yuan, and S. Feng, J. Am. Chem. Soc. **142**, 3316 (2020).

[35] J. Hilhorst, F. Marschall, T. N. Tran Thi, A. Last, and T. U. Schülli, J. Appl. Cryst. **47**, 1882 (2014).

[36] F. Marschall, A. Last, M. Simon, H. Vogt, and J. Mohr, Opt. Express **24**, 10880 (2016).

[37] N. Laanait, Z. Zhang, C. M. Schleputz, J. Vila-Comamala, M. J. Highland, and P. Fenter, J. Synchrotron Radiat. **21**, 1252 (2014).

[38] T. Zhou, T. Stankevic, A. Troian, Z. Ren, Z. Bi, J. Ohlsson, L. Samuelson, J. Hilhorst, T. Schulli, A. Mikkelsen, and O. Balmes, Microsc. Microanal. **24**, 128 (2018).

[39] E. Oksenberg, A. Merdasa, L. Houben, I. Kaplan-Ashiri, A. Rothman, I. G. Scheblykin, E. L. Unger, and E. Joselevich, Nat. Commun. **11**, 489 (2020).

[40] Y. Wang, X. Sun, R. Shivanna, Y. Yang, Z. Chen, Y. Guo, G. C. Wang, E. Wertz, F. Deschler, Z. Cai, H. Zhou, T. M. Lu, and J. Shi, Nano Lett. **16**, 7974 (2016).

[41] J. Chen, Y. Fu, L. Samad, L. Dang, Y. Zhao, S. Shen, L. Guo, and S. Jin, Nano Lett. **17**, 460 (2017).

[42] S. J. Leake, G. A. Chahine, H. Djazouli, T. Zhou, C. Richter, J. Hilhorst, L. Petit, M. I. Richard, C. Morawe, R. Barrett, L. Zhang, R. A. Homs-Regojo, V. Favre-Nicolin, P. Boesecke, and T. U. Schulli, J. Synchrotron Radiat. **26**, 571 (2019).

[43] See Supplemental Material at http://link.aps.org/supplemental/10.1103/PhysRevMaterials.6.054408 for a complete list of observed domain changes during temperature variation.

[44] D. Dzhigaev, Z. Zhang, L. A. B. Marçal, S. Sala, A. Björling, A. Mikkelsen, and J. Wallentin, New J. Phys. **23**, 063035 (2021).

[45] A. Yangui, M. Sy, L. Li, Y. Abid, P. Naumov, and K. Boukheddaden, Sci. Rep. **5**, 16634 (2015).

[46] P. Zou, C. Darie, C. V. Colin, and H. Klein, Inorg. Chem. **58**, 81 (2019).

[47] S. Liu, A. R. DeFilippo, M. Balasubramanian, Z. Liu, S. G. Wang, Y. S. Chen, S. Chariton, V. Prakapenka, X. Luo, L. Zhao, J. S. Martin, Y. Lin, Y. Yan, S. K. Ghose, and T. A. Tyson, Adv. Sci. **8**, 2003046 (2021).

[48] F. Haque and M. Mativenga, Phys. Status Solidi RRL **15**, 2100211 (2021).

[49] T. J. Whitcher, L. C. Gomes, D. Zhao, M. Bosman, X. Chi, Y. Wang, A. Carvalho, H. K. Hui, Q. Chang, M. B. H. Breese, A. H. Castro Neto, A. T. S. Wee, H. D. Sun, E. E. M. Chia, and A. Rusydi, NPG Asia Mater. **11**, 70 (2019).